High-resolution mosaic imaging with multifocal, multiphoton photon-counting microscopy

Eric Chandler,[1,*] Erich Hoover,[1] Jeff Field,[1] Kraig Sheetz,[1] Wafa Amir,[1]
Ramon Carriles,[1] Shi-you Ding,[2] and Jeff Squier[1]

[1]Center for Microintegrated Optics for Advanced Biological Control, Department of Physics, Colorado School of Mines,
1500 Illinois Street, Golden, Colorado 80401, USA

[2]National Renewable Energy Laboratory, 1617 Cole Boulevard, Golden, Colorado 80401, USA

*Corresponding author: echandle@mines.edu

Received 21 October 2008; revised 11 February 2009; accepted 13 February 2009;
posted 26 February 2009 (Doc. ID 102934); published 2 April 2009

High-resolution mosaic imaging is performed for the first time to our knowledge with a multifocal, multiphoton, photon-counting imaging system. We present a novel design consisting of a home-built femtosecond Yb-doped $KGdWO_4$ laser with an optical multiplexer, which is coupled with a commercial Olympus IX-71 microscope frame. Photon counting is performed using single-element detectors and an inexpensive electronic demultiplexer and counters. © 2009 Optical Society of America

OCIS codes: 030.5260, 180.5810, 180.4315.

1. Introduction

Multifocal, multiphoton microscopy at near-infrared (NIR) excitation wavelengths enables rapid image acquisition through efficient allocation of the laser light [1–3]. A single source beam with power greater than the damage threshold of a sample can be split into a number of beamlets, each of which can be used individually to generate an image. Various techniques of generating multiple foci for excitation include microlens arrays [1–7], etalon mirrors [8], beam splitter arrays [9–12], and diffractive optical elements (DOEs) [13,14]. Most techniques include time delays between adjacent foci to eliminate interference and consequently maintain the effective resolution of a single beam system. Most multifocal imaging systems are predominately image based, where a two-dimensional detector array such as a CCD is used to record the signal [1–6,8–10,12–14]. Unfortunately, image based detection is essentially limited to nonscattering specimens. Multianode photomultiplier tubes (MA-PMTs) have been used to address this issue and have effectively improved the sectioning without sacrificing image acquisition rates within scattering media [7,11]. However, the MA-PMT detection scheme does not fully mitigate the challenge of imaging in highly scattering media—scattered light can result in cross talk between detector elements.

We recently demonstrated multifocal, multiphoton imaging using single element detectors while operating in the photon-counting regime [15]. Thus traditional nonimaging detection is applicable even with scattering media and without loss of resolution. Notably, using these methods we demonstrated that dynamic imaging of multiple focal planes was possible for the first time by imaging the microorganism Euglena swimming in solution [16]. A second, novel capability of this imaging modality is that simultaneously imaging at orthogonal excitation polarizations is also possible as demonstrated with the previously developed system by imaging fluorescent microbeads and starch granules [15,16]. Further, we have imaged a trigeminal nerve from an adult mouse brain with a redesigned six-beam version of the previous microscope [17].

For highly polarized samples—materials with significantly different responses to orthogonally

0003-6935/09/112067-11$15.00/0

polarized excitation light—it is often desirable to image the same depth with both orthogonally polarized beams at the same time to provide a complete description of the sample.

The work presented here extends the application base of this previously developed imaging technology and explains in further detail the electronic demultiplexing and counting that forms the core of our photon-counting system. The signal conditioning and data acquisition system described are applicable to any microscope performing photon-counting detection with a pulsed laser as the illumination source.

First, we describe a home-built femtosecond Yb-doped $KGdWO_4$ laser for multifocal imaging applications. The output of this laser is coupled first into an optical multiplexer, then into an Olympus IX-71 microscope. The optical multiplexer design results in orthogonally polarized, time-delayed pulses that allow for multiple focal plane imaging. Galvanometric scan mirrors and a piezoelectric stage enable beam scanning, specimen scanning for mosaic imaging, or a combination of both. Using forward and back direction detectors, four images from two different depths are captured simultaneously. The signals generated from both depths are demultiplexed with field programmable gate arrays (FPGAs). We describe the signal conditioning external to the FPGAs, as well as the demultiplexing and counting performed with the FPGAs.

Additionally, we introduce an alternative method to alter the focal depth of one of the two beams of the optical multiplexer. Rather than use a deformable mirror as the end mirror in the optical multiplexer as in previous work [16], we place a lens of focal length f on a translation rail a distance f from the end mirror. Moving the lens along the rail changes the divergence of the beam without affecting the alignment. We can use this not only to change depth but also to compensate for the change in focal depth caused by the additional path length that the beam in the longer arm of the optical multiplexer travels. We quantify the focal depth offset by moving the sample in depth with the piezoelectric stage.

2. System Description

A. Yb:KGW Laser

Our Yb:KGW oscillator design is based on a laser developed by Major *et al.* [18]. A schematic is shown in Fig. 1. The pump source is a 25 W fiber coupled diode module with a 200 μm core diameter emitting at 980 nm (F25-980-2, Apollo Instruments, Inc.). The fiber output is imaged 1∶1 using two 40 mm singlets, L1 and L2, into a 4 mm long, 4 mm wide and 2 mm thick antireflection (AR) coated 5% Yb:KGW crystal (Eksma). The pump light enters the cavity through a short wave pass flat mirror, M2, coated for 98% transmission at the pump wavelength and 99.9% reflection at the laser wavelength. The crystal is cooled to 15 °C from two sides by thermoelectric coolers (TE Technology, Inc.) housed in a home-built water-cooled copper crystal mount.

Cavity elements include a 10% output coupler (CVI, Inc.), a pair of Gires–Tournois interferometer (GTI) mirrors (Layertec, GmbH) providing $-1300\,\text{fs}^2$ per bounce (four bounces per round trip per mirror), and two curved highly reflective (HR) (>99.98%) mirrors, M1 and M3, with a radii of curvature $r = 200$ mm (Layertec, GmbH). Mode locking is achieved by focusing the beam with a curved HR mirror, M4 ($r = 500$ mm, Layertec, GmbH), onto a semiconductor saturable absorber (SAM-1040-2-25.4g, Batop, GmbH) with a modulation depth of 1.2%.

At maximum pump power, the average output power is 2.5 W. Given our total cavity repetition rate of 56.5 MHz, this corresponds to average pulse energies of 45 nJ/pulse. The pulses are centered at 1040 nm and have a bandwidth of 4.9 nm. The pulse duration, as measured with a second-order intensity autocorrelator, is 242 fs full width at half-maximum (FWHM) when assuming a sech^2 pulse profile. The beam diameter at the output of the laser cavity is ~1 mm.

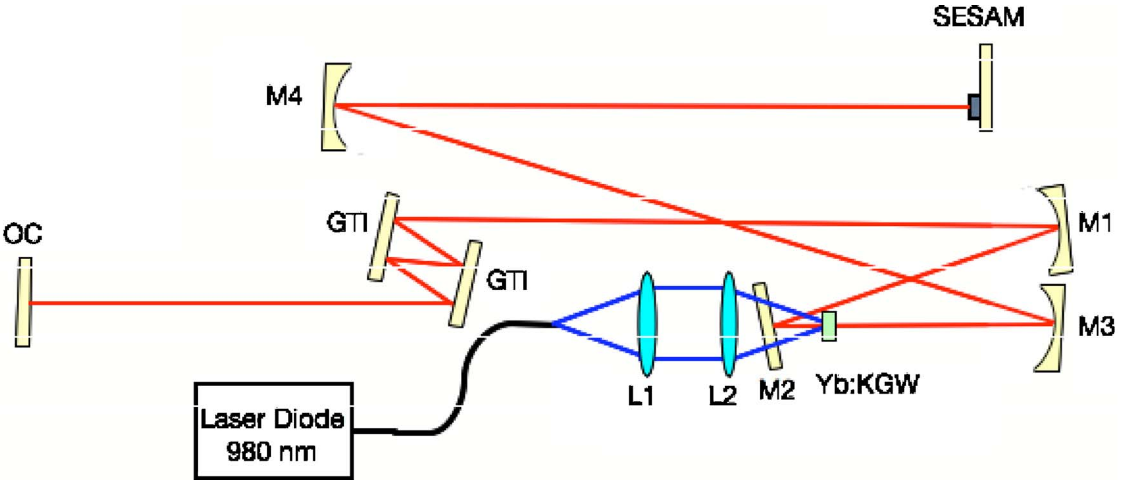

Fig. 1. (Color online) Schematic representation of Yb:KGW oscillator layout. Mirrors are labeled by M1–M4; L1 and L2, 40 mm singlet lenses; GTI, Gires–Tournois interferometer; OC, output coupler; SESAM, semiconductor saturable absorber mirror.

B. Optical Multiplexer

To enable simultaneous multidepth and multipolarization imaging, we have constructed an optical multiplexer (Fig. 2). We first rotate the output polarization of the laser 45° using a zero-order half-wave plate. The beam power is then split evenly along two paths with a polarizing beam splitter. One arm of the optical multiplexer is longer than the other by precisely the length corresponding to half the period of the laser. We place a lens in the longer arm of the optical multiplexer to alter the divergence of that beam. Zero-order quarter-wave plates are used in each arm so that the beams can be recombined on the polarizing beam splitter. At the output of the polarizing beam splitter, the laser repetition rate is effectively 113 MHz—twice the original repetition rate —and sequential pulses alternate between orthogonal linear polarization states. We monitor the output frequency of the optical multiplexer with a glass pickoff slide and a photodiode (Thor Labs model DET210).

After the optical multiplexer, there are two available paths for the interlaced pulse train to travel, each of which enables a different scanning modality. We can use a set of galvanometric scan mirrors (GSI Lumonics, model SC-2000) to quickly raster the beam at the focus of the objective. Unfortunately, the scan mirror casing limits the output beam diameter to be smaller than the input aperture of our Olympus UPlanSApo 20x/0.75 NA (14 mm input aperture) imaging objective. Alternatively, we can raster the sample while keeping the beam stationary and overfill the back of the imaging objective. However, this scanning modality requires six minutes per scan when stepping the stage and is intended for fixed specimens and samples. The stage can be programmed for continuous movement, reducing the scan time to approximately 4 seconds, but introducing uncertainty into the sample position (as a result of the acceleration of the stage).

For high speed scanning, the output of the optical multiplexer is sent through an $f:2f$ telescope to expand the beam. The beam then travels into a set of galvanometric scan mirrors, controlled via serial communication in LabVIEW by a desktop computer. These scan mirrors can reliably scan at frame rates up to 10 Hz, generating images of 128 lines and 128 pixels per line. The scan time can be increased in software for longer pixel dwell times, which builds up photon counts to improve image contrast as needed. The scanners are placed at a telecentric image plane relative to the back of the excitation objective within the Olympus IX-71 microscope.

For high resolution scanning, a pair of flip mirrors (M1, M2) are used to direct the beam through a

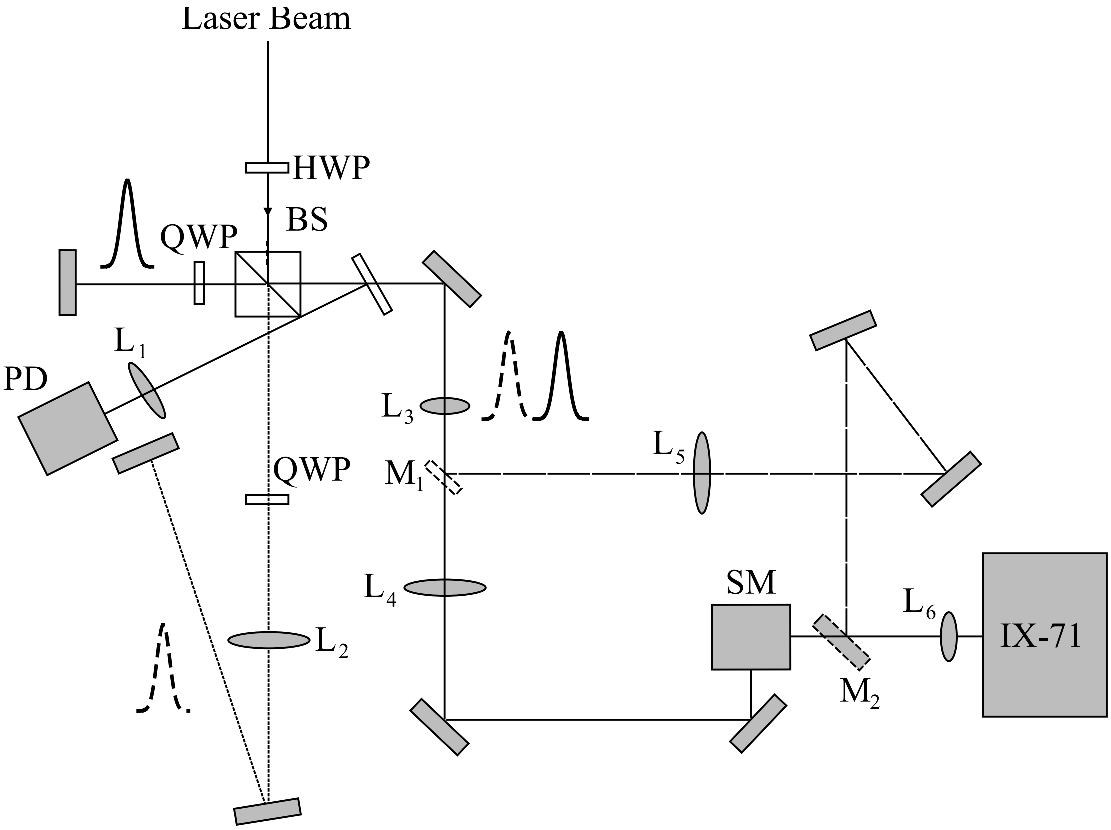

Fig. 2. Schematic representation of the optical multiplexer and scan optics, not to scale: HWP, half-wave plate; QWP, quarter-wave plate; BS, polarizing beam splitter; PD, photodiode; SM, scan mirrors; L1 and L3, 5 cm; L2, 70 cm; L4, 10 cm; L5, 21 cm; L6, 18 cm lenses. M1 is a flip mirror, redirecting the beam to a $f:4f$ telescope to further expand the beam, bypassing the scan mirrors. M2 is a silver mirror on a kinematic mount to direct the expanded beam into the IX-71.

nonscanning arm. In this arm, the beam is expanded by an $f:4f$ telescope. This is to better match the Olympus 0.75 NA objective. We then raster the sample over 128 lines with 128 steps per line.

C. Olympus IX-71

The Olympus IX-71 is a commercial inverted research microscope, equipped with a 0.55 NA condenser lens positioned above the sample for white-light imaging. The excitation beam from the multiplexer is coupled through the left side port. Inside the microscope body, the beam is reflected upward and passes through a tube lens (focal length 180 mm) into the back of the excitation objective.

Within the IX-71, a dichroic mirror (Chroma 725dcxr) placed between the internal tube lens and the objective at 45° angle of incidence reflects wavelengths below 700 nm at greater than 90% efficiency through a second port on the right side, enabling epidetection. For low resolution imaging, an Olympus UPlanSApo 20 × /0.75 NA objective is used for excitation, while a matching objective is used for collection. The back entrance pupil of these objectives is 14 mm; therefore an expanded beam is required to take full advantage of the NA. For higher resolution imaging, an Olympus UPlanSApo 60 × /1.35 NA oil immersion objective is used for excitation, while the Olympus 0.75 NA objective is used for collection. Both objectives are corrected for 170 μm of glass.

Additionally, we use a piezoelectric stage (Mad City Labs Nano-view/M200-3) atop the Olympus micrometer-controlled sample stage for nanometer precision sample positioning. The NanoStage is precise to within 0.4 nm, with a range of 0–200 μm along all three spatial directions. We thus have the flexibility to generate images either by sample scanning or beam rastering.

Signal collection is performed with a pair of photomultiplier tubes (PMTs). We use a Hamamatsu R5600U-3 in transmission and a Hamamatsu H7422P-40MOD in the back direction. To isolate the signal from the fundamental light and from other wavelengths, we use a BG-39 filter in front of each PMT. Since we can generate second-harmonic and third-harmonic light as well as multiphoton excitation fluorescence (MPEF) simultaneously, we must use additional filters to further isolate the signal of interest. We use UG-1 glass for third-harmonic generation (THG) imaging and a Chroma ET525/50 m-2 p filter for second-harmonic generation (SHG).

D. Electronic Demultiplexer

When the interlaced pulse train of 113 MHz (~8.8 ns between pulses) encounters the sample, a nonlinear signal—SHG, THG, or MPEF—is generated, and the resulting photons are detected by the PMTs in the forward and backward directions. Since SHG and THG are instantaneous processes, and MPEF has a typical fluorescence lifetime of a few nanoseconds, the signal photon detected by the PMT must come from the last pulse to excite the sample. This allows us to match the PMT pulse with the signal from the incoming pulse train (Fig. 3) that we observe with the photodiode (Fig. 2), which provides our master clock signal for the FPGA.

The signal "jitter"—variability in signal timing—that occurs with MPEF (Fig. 3) is the predominant source of image "bleedthrough," where information from one depth leaks into the other depth. This is caused when the signal photon generation is delayed by more than the bin width. "Bleedthrough" due to a highly scattering sample—where the signal photon is delayed by traversing extra distance—is extremely unlikely, as the signal pulse would have to be delayed by over 8 ns (2.4 m) with harmonic generation (an instantaneous process) and for an average MPEF lifetime of ~6 ns, a delay of 2 ns (0.6 m) would be required. The length the delayed signal photon must traverse is far greater than the thickness of any sample that would be imaged in our apparatus.

To generate our images, the PMT signal—which contains the data from both depths—must be demultiplexed and counted. Demultiplexing the simultaneously acquired images in software requires substantial computational resources and sampling rates of at least tens of GHz. Thus software demultiplexing prohibits real-time analysis. For this

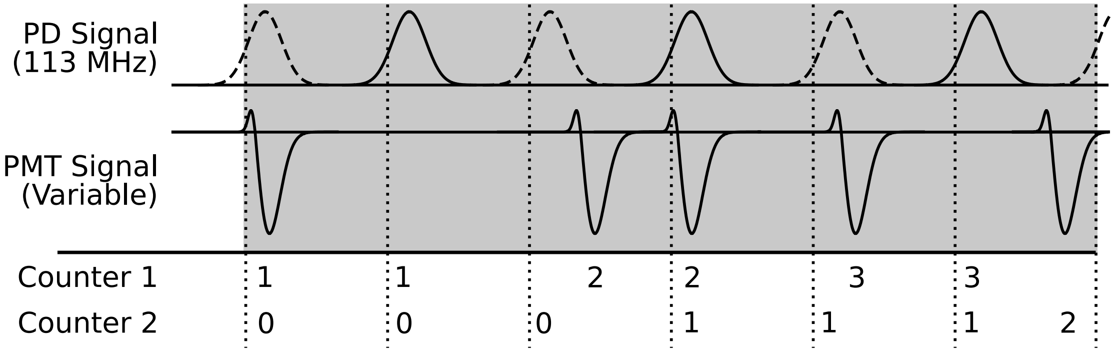

Fig. 3. Pulse sequence from both the photodiode and the PMT. The photodiode registers twice the laser frequency, as the interlaced pulse train contains two pulse trains of 56 MHz at orthogonal polarizations, designated by the dashed and solid curves. The PMT signal, with some variation in timing within a bin, is meant to simulate a MPEF response. The signal counters increment when a PMT pulse occurs between one clock cycle and the next.

reason, we opted for hardware demultiplexing implemented through a FPGA. This solution combines the fast response times of hardware with the flexibility of easily changing the hardware architecture.

We use an Altera DE2 board with a Cyclone II FPGA. The FPGA is programmed with the very high speed integrated circuit (VHSIC) hardware description language (VHDL, IEEE 1164). Due to its low cost and high bandwidth (up to ~400 MHz), the DE2 is an optimal device for decoding the signals from our microscope.

To register a photon count, we must convert the analog signal output of the PMT to a digital input signal to the FPGA. This conversion involves two steps: first using a discriminator to reject low voltage noise pulses, then generating a transistor-transistor logic (TTL) HI pulse for analog input pulses that exceed the discriminator threshold.

We reduce the cost of the hardware required for demultiplexing the signals as compared to our previous work [16] by altering the circuitry to amplify and convert the signal from small analog voltages (10–100 mV) to low voltage TTL (LVTTL) signals (0–2.0 V) readable by the FPGA, as shown in Fig. 4. We amplify the output of each PMT by a factor of ~30 with a high-speed coaxial pulse amplifier (Mini-Circuits ZPUL-30P). The output of the pulse amplifier is still an analog signal, which is then directed into a dual-channel comparator (Pulse Research Lab PRL-350TTL). The comparator simultaneously performs both the thresholding and analog to LVTTL signal conversion. The amplified analog signal is sent to the inverting input of the comparator, while a DC voltage—our threshold voltage—is applied to the noninverting input. The comparator acts as a programmable discriminator, railing to its maximum output voltage of 2.2 V when the incoming signal voltage is above the threshold voltage. The positive LVTTL pulses output from the comparator can then be read by the FPGA and counted, as shown in Fig. 3. Since the FPGA acts as a counter, we further reduce the cost of the electronics by eliminating the need for a photon-counting module. Each PMT requires an individual FPGA to generate a pair of images.

The DE2 board accepts four signals to generate an image: the photodiode signal (laser clock), the PMT signal, a pixel clock, and a line clock. The 113 MHz laser clock pulse train acts as a toggle between two data bins, activating one bin and deactivating the other with each pulse. While a bin is active, it will increment a counter if a signal pulse is detected. This data bin toggling and signal pulse counting continues until the rising edge of a pixel clock pulse is detected. At the end of each pixel, the final counter value of each bin is stored and reset to zero. After 128 pixels have been read, the leading edge of the line clock indicates the start of a new line, and the pixel clock is reset to zero. Each image is then a 128 × 128 pixel intensity map, scaled in units of photon counts. In order to take advantage of the Cyclone II FPGA's optimized 16-bit counters, each pixel is limited to a 16-bit number—a maximum of 2^{16}, or 65536 photons, per pixel.

With the scan mirrors, a pixel and line clock is automatically generated from the scan driver module. The frequencies of the pixel and line clocks are programmable. When the Nano-view stage is used to scan, we must fabricate pixel and line clocks with a data acquisition (DAQ) card (National Instruments) via LabVIEW.

We are able to acquire many images in sequence by taking advantage of the built-in static random access

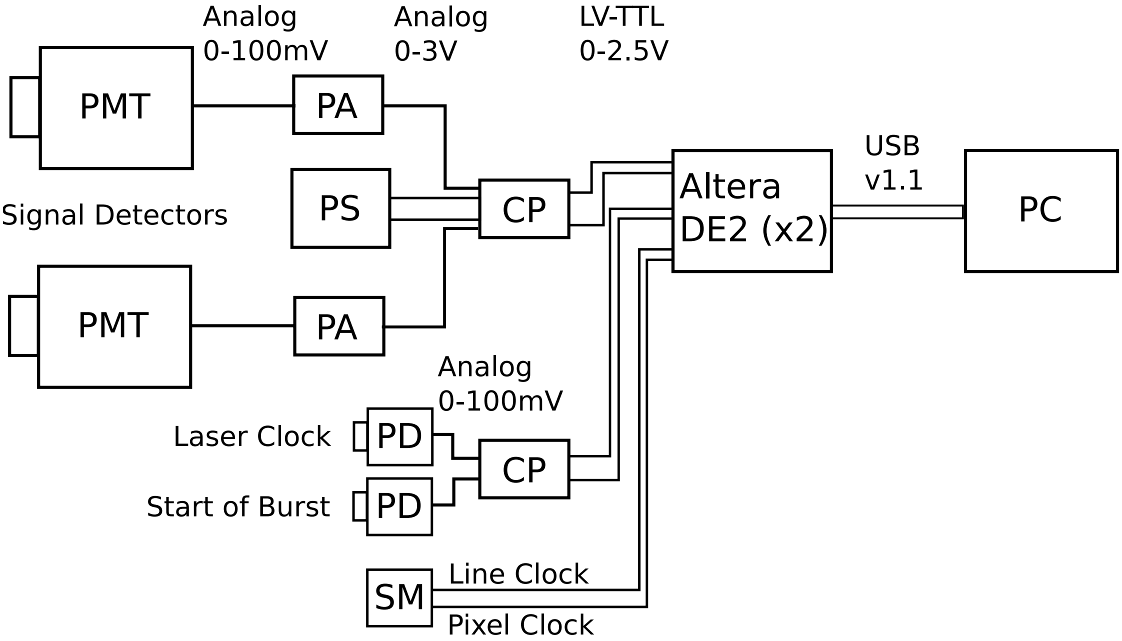

Fig. 4. Detection and demultiplexing electronics: PMT, photomultiplier tube; PA, pulse amplifier; PS, power supply; CP, comparator; PD, photodiode; SM, scan mirror driver; PC, personal computer. Each separate PMT signal is directed to a different DE2 board.

memory (SRAM) and synchronous dynamic random access memory (SDRAM) on the DE2 board. The board handles only universal serial bus (USB) 1.1 data transfer rates; therefore we cannot transmit data after each pixel, or even each line, to the computer via USB. We buffer a line of data in the SRAM until the line is completed and then transfer that line to a processor loaded onto the FPGA (Altera's NIOS II) while we simultaneously acquire the next line of data. The processor buffers these lines of data to the SDRAM on the DE2 board and assembles a complete image on board. The completed image is then transferred via USB to the computer while the next image is being captured. The computer then stores each image in separate files containing the photon count at each pixel. Since each scan is composed of data from two depths, two separate image files are stored per scan—one for each depth.

The electronic system as a whole affords a great deal of flexibility with regard to the frequency of the source laser. The slowest device is the comparator, which has a maximum operating frequency of 250 MHz—over twice our laser clock frequency.

Signal distortion from external electromagnetic radiation is a significant problem at these frequencies. In order to overcome this issue, we use double-shielded RG-223 cable and threaded subminiature version A (SMA) connectors where possible to limit external interference and reduce cross talk. Use of shielded cable allows the use of a lower threshold voltage on the comparator, as there are fewer noise pulses generated from external electromagnetic events, and these noise pulses have smaller amplitudes than with standard unshielded RG-58 cable with Bayonet Neill Concelman (BNC) connectors. For example, lowering the threshold from 0.35 V to 0.20 V allowed us to observe two to four times as many counts per image.

Although a lower comparator threshold allows more signal counts through, it also passes additional background counts. The typical number of background counts per pixel-second provides a good figure of merit for noise, as the average number of background counts per pixel varies with the total scan time. This figure was obtained by performing a 12 second scan with the beam blocked and a comparator threshold of 0.15 V. Detecting THG in the forward direction and SHG in the back direction using the filters previously described, we obtain a total of 0.000837 and 0.44375 counts per pixel-second for the two detectors, respectively.

It was observed that of all of the 113,000,000 laser clock pulses/second, the FPGA would occasionally fail to count one or more. When this occurred, the images at two separate depths would "flip"—data generated from one depth would appear in the image corresponding to the other depth. For further protection against such laser clock errors, we have instituted a "start of burst" clock signal. The "start of burst" is obtained from a photodiode in the laser cavity, yielding a 56.5 MHz reference clock. We time the pulses from this clock to occur before one of the pulses on the 113 MHz laser clock. The "start of burst" indicates to the DE2 that the following clock pulse will correspond to the first counter. This prevents data sets from flipping in the middle of a scan due to loss of a clock pulse—at worst, a laser pulse is misrepresented.

Previously, we were also unable to identify which image of the pair would be generated from one arm of the optical multiplexer or the other, as it would depend on which clock pulse was the first detected when a scan was initiated. The "start of burst" locks the image sequence so one arm of the optical multiplexer always corresponds to a particular image—for example, the pulses from the short arm of the optical multiplexer will always generate "image 1."

3. Beam Scanning and Focal Depth Control

A. Beam Scanning

We are capable of generating images at rates up to 10 frames per second with a set of SC-2000 GSI Lumonics scan mirrors. In Fig. 5, we image crystalline cellulose with an Olympus UPlanSApo 20x/0.75 NA objective with 12 mW time-averaged power at the focus per beam. The crystalline cellulose is mounted between two 170 μm 2 in.×1 in. (5 cm×2.5 cm) coverslips, and is deposited on the slide by evaporation of a liquid solution containing the crystals. The scan time per frame is 12 seconds, yielding a pixel dwell time of 0.7 ms. All images are 128 × 128 pixels. SHG was captured in the back direction, and images at orthogonal excitation polarizations are shown in Figs. 5(a) and 5(b). THG was captured in transmission, also at orthogonal polarizations, and images are shown in Figs. 5(c) and 5(d).

B. Focal Depth Control

We are able to adjust the divergence of one of the two interlaced beams simply by adjusting the position of a lens with focal length f with respect to an end mirror nominally f away. We use a 700 mm lens on a translation rail (Newport model PRL-12) in the long arm of the optical multiplexer. We first adjust the lens position to focus the two interlaced beams at the same depth. Each beam nominally focuses to different depths, given that the different arm lengths in the optical multiplexer result in a slightly different diameter for each beam at the back of the imaging objective. We then offset the lens position to focus one of the interlaced beams at a different depth by moving the lens away from the end mirror.

We demonstrate the focal plane adjustment by imaging gold nanodisks that are 250 nm in diameter, 20 nm thick, and spaced 2 μm apart in a square grid. These disks are created by electron beam lithography directly atop a glass coverslide. In Fig. 6 we image these nanodisks, collecting epi-SHG. We image with 10 mW time-averaged power at the focus and sum ten 12 second scans to build up contrast in the images shown. As with all images obtained with

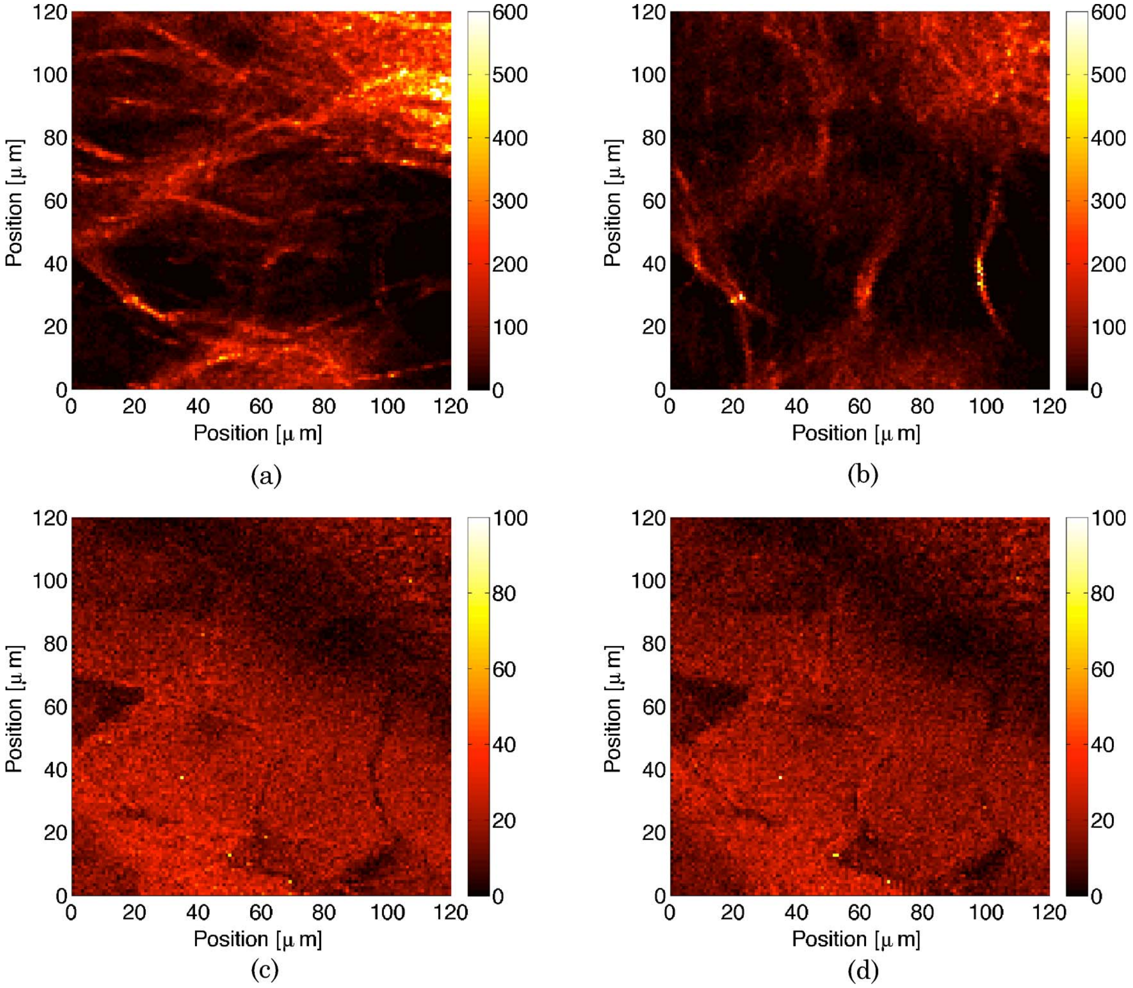

(a)
(b)
(c)
(d)

Fig. 5. (Color online) Crystalline cellulose imaged with (a), (b) epi-SHG at orthogonal polarizations, and (c), (d) transmission THG at orthogonal polarizations. Top and bottom image pairs are generated from the same excitation polarization. All images are scaled in photon counts.

our technique, they are 128 × 128 pixels. In Figs. 6(a) and 6(b), we image these nanodisks when translating the focus of the second beam, shown in (b), by 13 μm in depth. In Figs. 6(c) and 6(d), we step the sample in depth with the Nano-view piezoelectric stage by 13 μm, bringing the nanodisks into focus with the second beam. The difference in maximum photon counts between the two orthogonal excitation polarizations [Figs. 6(a) and 6(d)] is due to the strong polarization dependence of the nanodisks [19].

We also use the Nano-view piezoelectric stage to determine how far we can offset one focus from another. For our selected lens focal length, each additional 1 cm that the lens is moved away from the end mirror (from the depth matching rail position) corresponds to a change of 1 μm in focal depth. Given the geometry of the optical multiplexing optics, the maximum focal offset we can achieve is 14 μm.

This single lens technique only alters the focal depth of one of the two orthogonally polarized beams—it does not compensate for spherical or chromatic aberrations. An adaptive optic, such as the deformable mirror used in previous work, would be more appropriate when aberrations or pulse control is a consideration [16].

C. Point Spread Function Characterization

We use the same gold nanodisks as in the previous subsection to experimentally estimate the point spread function of our microscope system. We raster the sample over 10 μm, then step 1 μm in depth and repeat. We image with 4 mW time-averaged power per beam at the focus of the objective, detecting THG in the forward direction and SHG in the back direction.

The experimentally determined beam waist and confocal parameter when overfilling the imaging objective (Olympus UPlanSApo 20 × /0.75 NA) are 1.01 μm and 4.36 μm, respectively. These are ~20% larger than the values obtained from Eqs. (1) and (2), representing the beam waist and confocal parameter, respectively, which are 0.846 μm and 3.70 μm [20]. Since we are not imaging these nanodisks through 170 μm of coverslip as required by the objective, we are introducing spherical aberration, which would contribute to a larger focal volume.

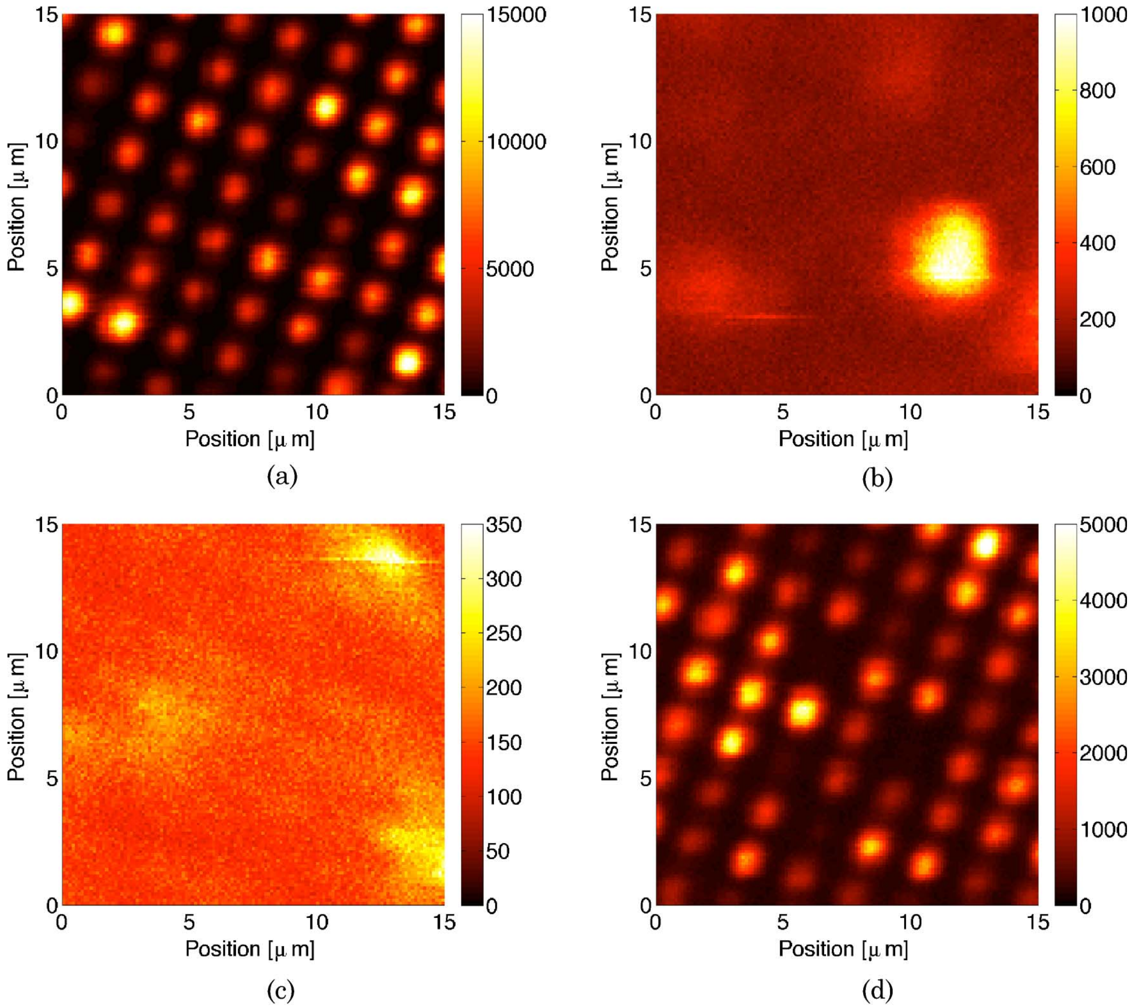

(a) (b) (c) (d)

Fig. 6. (Color online) Epi-SHG images of gold nandisks in (a) and (b) when the second beam focus is translated in depth by 13 μm. Images in (c) and (d) are generated when the piezoelectric stage is moved 13 μm in depth. Top and bottom image pairs are generated from the same excitation polarization. All images are scaled in units of photon counts.

$$\mathrm{FWHM}_{\mathrm{lateral}} = \frac{0.61\lambda}{\mathrm{NA}}, \tag{1}$$

$$\mathrm{FWHM}_{\mathrm{axial}} = \frac{2n\lambda}{\mathrm{NA}^2}. \tag{2}$$

4. Mosaic Imaging

The high-precision piezoelectric stage offers the capability of "stitching" together several images in the same plane to form a larger composite image. Because we are limited to 128 pixels per line, scanning a larger area decreases resolution by increasing the step size per pixel. By "stitching" together an image, we are able to explore a larger area without losing resolution.

We use the Nano-view stage to generate nine individual scans of 30 × 30 μm. We trim 5 μm from overlapping edges to create a composite image of total area 80 × 80 μm. With simultaneous forward and back direction imaging, as well as two incident polarizations, we generate four images with a single scan. We use the same nanocrystalline cellulose strands, mounted between two 170 μm thick 2 in.×1 in. cover slips, as our sample. We image at 0.75 NA with 6 mW time-averaged power per interlaced beam at the focus. In Fig. 7(a), we show all nine images (epi-SHG) as generated by a single excitation polarization. The composite of those nine individual images is shown in Fig. 7(c). Another epi-SHG image, generated with the orthogonal excitiation polarization, is shown in Fig. 7(b). THG was collected in transmission to generate Figs. 7(d) and 7(e).

Additionally, we demonstrate mosaic imaging at high (1.35) NA in Fig. 8. We collect epi-SHG signals from two orthogonal excitation polarizations simultaneously to generate Fig. 8, using 6 mW time-averaged power per beam at the focus. These images are also 80 μm × 80 μm in scale.

5. Conclusions

We have demonstrated the extensive capabilities of our microscope, created by coupling a home-built Yb:KGW laser to a commercial Olympus IX-71 microscope frame. We demonstrate the capabilities

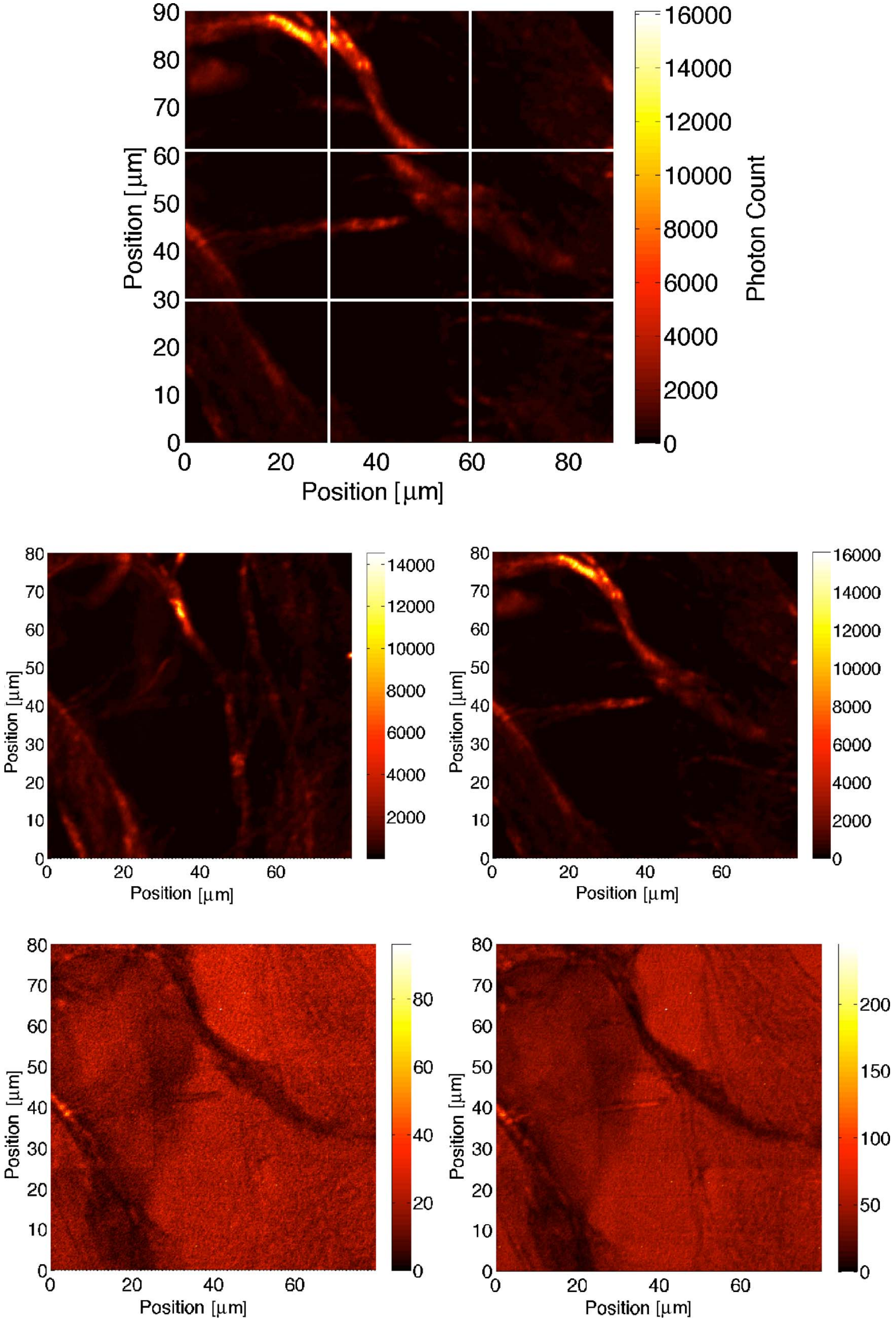

Fig. 7. (Color online) Example of mosaic imaging. Nine individually acquired 30 μm × 30 μm epi-SHG images are shown in (a). The corresponding "stitched" together image is shown in (c). An epi-SHG image for the orthogonal excitation polarization is shown in (b). Transmission THG images are shown in (d) and (e). Left and right image pairs are generated from the same excitation polarization. All images are scaled in photon counts.

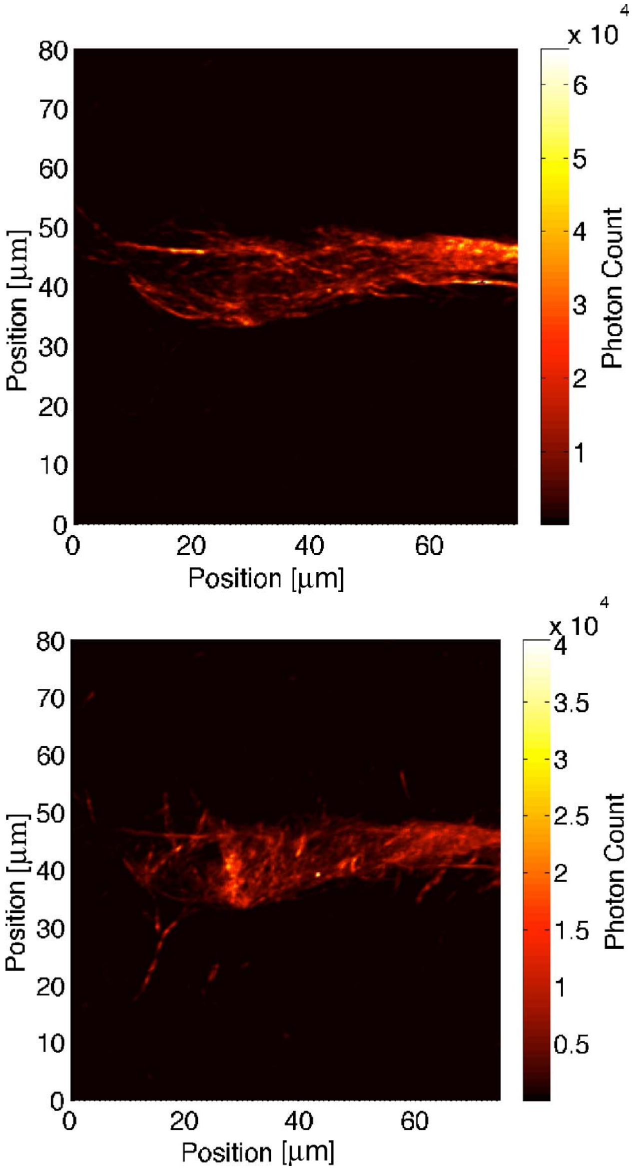

Fig. 8. (Color online) Epi-SHG mosaic images of crystalline cellulose imaged at 1.35 NA, imaged simultaneously at two orthogonal polarizations. These images are also composed of nine individual scans.

of FPGAs and digital comparators to simplify the signal conditioning and detection. This system offers great flexibility and cost reduction as compared to conventional photon-counting techniques. We have also shown that, under the limitation of being unable to correct for aberrations, we can substitute a simple lens for a deformable mirror to obtain a focal plane displacement. Further, we have characterized this system by examining gold nanodisks and extracting the beam radius at the focus and confocal parameter. Additionally, we have shown the utility of a high-precision piezoelectric stage by automatically scanning smaller areas at high resolution, and stitching together individual scans to generate a composite image.

We would like to acknowledge and thank the National Renewable Energy Laboratory for support. This work was supported under NREL subcontract ZCO-7-77379. Additionally, we would like to thank Professor Martti Kauranen of the Tampere University of Technology for the loan of the gold nanostructures used to characterize the beam focus in this study.

References

1. J. Bewersdorf, R. Pick, and S. Hell, "Multifocal multiphoton microscopy," Opt. Lett. **23**, 655–657 (1998).
2. M. Straub and S. Hell, "Multifocal multiphoton microscopy: a fast and efficient tool for 3-D fluorescence imaging," Bioimaging **6**, 177–185 (1998).
3. A. Egner and S. Hell, "Time multiplexing and parallelization in multifocal multiphoton microscopy," J. Opt. Soc. Am. A **17**, 1192–1201 (2000).
4. A. Buist, M. Müller, J. Squier, and G. Brakenhoff, "Real time two-photon absorption microscopy using multi-point excitation," J. Microsc. (Oxford) **192**, 217–226 (1998).
5. K. Bahlmann, P. So, M. Kirber, R. Reich, B. Kosicki, W. McGonagle, and K. Bellve, "Multifocal multiphoton microscopy (MMM) at a frame rate beyond 600 Hz," Opt. Express **15**, 10991 (2007).
6. V. Andresen, A. Egner, and S. Hell, "Time-multiplexed multifocal multiphoton microscope," Opt. Lett. **26**, 75–77 (2001).
7. K. Kim, C. Buehler, K. Bahlmann, T. Ragan, W. Lee, E. Nedivi, E. Heffer, S. Fantini, and P. So, "Multifocal multiphoton microscopy based on multianode photomultiplier tubes," Opt. Express **15**, 11658–11678 (2007).
8. D. Fittinghoff and J. Squier, "Time-decorrelated multifocal array for multiphoton microscopy and micromachining," Opt. Lett. **25**, 1213–1215 (2000).
9. R. Niesner, V. Andresen, J. Neumann, H. Spiecker, and M. Gunzer, "The power of single and multibeam two-photon microscopy for high-resolution and high-speed deep tissue and intravital imaging," Biophys. J. **93**, 2519–2529 (2007).
10. J. Martini, K. Schmied, R. Palmisano, K. Toensing, D. Anselmetti, and T. Merkle, "Multifocal two-photon laser scanning microscopy combined with photo-activatable GFP for *in vivo* monitoring of intracellular protein dynamics in real time," J. Struct. Biol. **158**, 401–409 (2007).
11. S. Kumar, C. Dunsby, P. De Beule, D. Owen, U. Anand, P. Lanigan, R. Benninger, D. Davis, M. Neil, P. Anand, C. Benham, A. Naylor, and P. French, "Multifocal multiphoton excitation and time correlated single photon counting detecting for 3-D fluorescence lifetime imaging," Opt. Express **15**, 12548–12561 (2007).
12. D. Fittinghoff, C. Schaffer, E. Mazur, and J. Squier, "Time-decorrelated multifocal micromachining and trapping," IEEE J. Sel. Top. Quantum Electron. **7**, 559–566 (2001).
13. J. Jureller, H. Kim, and N. Scherer, "Stochastic scanning multiphoton multifocal microscopy," Opt. Express **14**, 3406–3414 (2006).
14. L. Sacconi, E. Froner, R. Antolini, M. Taghizadeh, A. Choudhury, and F. Pavone, "Multiphoton multifocal microscopy exploiting a diffractive optical element," Opt. Lett. **28**, 1918–1920 (2003).
15. W. Amir, R. Carriles, E. Hoover, T. Planchon, C. Durfee, and J. Squier, "Simultaneous imaging of multiple focal planes using a two-photon scanning microscope," Opt. Lett. **32**, 1731–1733 (2007).
16. R. Carriles, K. Sheetz, E. Hoover, J. Squier, and V. Barzda, "Simultaneous multifocal, multiphoton, photon counting microscopy," Opt. Express **16**, 10364–10371 (2008).
17. K. Sheetz, E. Hoover, R. Carriles, D. Kleinfeld, and J. Squier, "Advancing multifocal nonlinear microscopy: development

and application of a novel multibeam Yb:KGd(WO4)2 oscillator," Opt. Express **16**, 17574–17584 (2008).

18. A. Major, R. Cisek, and V. Barzda, "Femtosecond Yb:KGd$(WO_4)_2$ laser oscillator pumped by a high power fiber-coupled diode laser module," Opt. Express **14**, 12163–12168 (2006).
19. B. Canfield, H. Husu, J. Kontio, J. Viheriälä, T. Rytkönen, T. Niemi, E. Chandler, A. Hrin, J. Squier, and M. Kauranen, "Inhomogeneities in the nonlinear tensorial responses of arrays of gold nanodots," New J. Phys. **10**, 013001 (2008).
20. M. Müller, *Introduction to Confocal Fluorescence Microscopy* (SPIE, 2006).